

A major purpose of the Technical Information Center is to provide the broadest dissemination possible of information contained in DOE's Research and Development Reports to business, industry, the academic community, and federal, state and local governments.

Although a small portion of this report is not reproducible, it is being made available to expedite the availability of information on the research discussed herein.

1

NOTICE

PORTIONS OF THIS REPORT ARE ILLEGIBLE. It has been reproduced from the best available copy to permit the broadest possible availability.

Los Alamos National Laboratory is operated by the University of California for the United States Department of Energy under contract W-7405-ENG-36

CONF-8405164--3

TITLE TWO-FIELD AND DRIFT-FLUX MODELS WITH APPLICATIONS TO NUCLEAR REACTOR SAFETY

LA-UR--84-1650

DE84 012456

AUTHOR(S) J. R. Travis

SUBMITTED TO IAEA Technical Committee/Workshop on the Uses of Computer Codes for Nuclear Reactor Safety Analysis, Varna, Bulgaria, 28 May - 1 June 1984.

DISCLAIMER

This report was prepared as an account of work sponsored by an agency of the United States Government. Neither the United States Government nor any agency thereof, nor any of their employees, makes any warranty, express or implied, or assumes any legal liability or responsibility for the accuracy, completeness, or usefulness of any information, apparatus, product, or process disclosed, or represents that its use would not infringe privately owned rights. Reference herein to any specific commercial product, process, or service by trade name, trademark, manufacturer, or otherwise does not necessarily constitute or imply its endorsement, recommendation, or favoring by the United States Government or any agency thereof. The views and opinions of authors expressed herein do not necessarily state or reflect those of the United States Government or any agency thereof.

MASTER

By acceptance of this article, the publisher recognizes that the U.S. Government retains a nonexclusive, royalty-free license to publish or reproduce the published form of this contribution, or to allow others to do so, for U.S. Government purposes. The Los Alamos National Laboratory requests that the publisher identify this article as work performed under the auspices of the U.S. Department of Energy.

Los Alamos Los Alamos National Laboratory Los Alamos, New Mexico 87545

TWO-FIELD AND DRIFT-FLUX MODELS WITH APPLICATIONS TO NUCLEAR REACTOR SAFETY

J. R. Travis

Theoretical Division, Group T-3
University of California
Los Alamos National Laboratory
Los Alamos, New Mexico 87545

ABSTRACT

The ideas of the two-field (6 equation model) and drift-flux (4 equation model) description of two-phase flows are presented. Several example calculations relating to reactor safety are discussed and comparisons of the numerical results and experimental data are shown to be in good agreement.

I. INTRODUCTION

In many reactor safety problems, the presence of several phases such as bubbles, chunks, or droplets immersed in a continuous fluid introduces the possibility of time-dependent relative motion, and accordingly, the mathematical description requires more than one set of field variables to adequately specify the dynamics. The two-field or six-equation model offers the most comprehensive and detailed description of two-phase fluid dynamics [1]. It is based on separate sets of field equations governing the two-phase dynamics. The model is formulated on six conservation equations, i.e., mass, momentum, and energy for each phase, coupled through the condition of pressure equilibrium between phases, equation of state data, and the three required constitutive relationships for interfacial exchange of mass, momentum, and energy.

For many problems in reactor safety analysis, the full two field model may be simplified for a two-phase mixture in the drift-flux approximation. In this model, the fluid is treated as an inhomogeneous mixture with terms describing motions of the center of mass and the deviations due to relative phasic velocities [1].

We will briefly present the mathematical models and then apply them in their numerical approximation to a few examples.

II. MATHEMATICAL MODELS

In the multifield formulation, each phase is governed by a separate set of field equations for mass

$$\frac{\partial \rho^i}{\partial t} + \nabla \cdot (\rho^i \bar{u}^i) = S_{\rho}^i \quad (1)$$

momentum

$$\frac{\partial (\rho^i \bar{u}^i)}{\partial t} + \nabla \cdot (\rho^i \bar{u}^i \bar{u}^i) = -\alpha^i \nabla P + K(\bar{u}^i - \bar{u}) + \rho^i \bar{g} + \bar{V} + \bar{S}_m^i \quad (2)$$

and specific internal energy density

$$\frac{\partial (\rho^i I^i)}{\partial t} + \nabla \cdot (\rho^i \bar{u}^i I^i) = \frac{\alpha^i}{\rho} \left[\frac{\partial \rho}{\partial t} + \bar{u} \cdot \nabla \rho \right] + R(\bar{T}^i - \bar{T}) + \nabla \cdot (k \alpha^i \nabla T) + \Lambda + V_i^i + S_i^i \quad (3)$$

The equation-of-state may be expressed as $\rho = \rho(p, I)$, $T = T(p, I)$, or $p = p(\rho, I)$, $T = T(\rho, I)$, in which the microscopic density, ρ , is related to the macroscopic density, ρ^i , and the volume fraction, α , by $\rho = \rho^i / \alpha$. It is implicit in this formulation that summing the volume fractions over all fields is identically equal to unity.

In Eqs. (1-3), interactions between the phases due to phase transitions are described by S_{ρ}^i , \bar{S}_m^i , and S_i^i which are respectively, sources or sinks of mass, momentum, and internal energy density. Additional coupling between the phases exists through the effective drag function K , where \bar{u} is the mean relative velocity for the phase, and the energy exchange function R , where \bar{T} is the mean exchange temperature for that field. Other terms account for the effects of viscous stress, \bar{V} , viscous work V_i^i , and the rate of production of internal energy density due to momentum exchange, Λ .

A numerical method for the transient, two-dimensional, two-phase solution of Eqs. (1-3), with the assumption that the liquid is incompressible, was first proposed by Harlow and Amsden [2] and implemented in the KACHINA code [3]. The field equations are implicitly coupled in their numerical representation to allow for strong interfacial momentum interactions and use is made of the Implicit Continuous-fluid Eulerian (ICE) technique [4] to allow for both low-speed and high-speed flow calculations. The resulting numerical technique is referred to as the Implicit Multi-Field (IMF) method. K-FIX (KACHINA-Fully Implicit EXchange functions) [5] followed KACHINA with the following improvements: (1) full compressibility in both fields, (2) implicit calculation of the void fraction, and (3) implicit calculation of the phase velocities with the field equations.

The source terms for the liquid field equations in K-FIX are:

$$(S_p)_l = J_c - J_e,$$

where J_e and J_c denote the mass transfer per unit time and volume due to vaporation and condensation, respectively;

$$(\bar{S}_m)_l = J_c \bar{u}_v - J_e \bar{u}_l,$$

where \bar{u}_v and \bar{u}_l represent the vapor and liquid velocities, respectively (Note that the velocity of the donor material is used in this momentum relationship as a first order approximation to the effective mixing velocity at the vapor-liquid interface); and

$$(S_i)_l + \frac{\alpha_l p}{\rho_l} \left[\frac{\partial \rho_l}{\partial t} + \bar{u}_l \cdot \nabla \rho_l \right] = - (J_e - J_c) h_v - p \left[\frac{\partial \alpha_l}{\partial t} + \nabla \cdot (\alpha_l \bar{u}_l) \right],$$

where h_v is the specific enthalpy of the vapor. The source terms for the vapor field are written in similar

fashion as $(S_p)_v = J_e - J_c$, $(\bar{S}_m)_v = J_e \bar{u}_l - J_c \bar{u}_v$, and $(S_i)_v + \frac{\alpha_v p}{\rho_v} \left[\frac{\partial \rho_v}{\partial t} + \bar{u}_v \cdot \nabla \rho_v \right] = (J_e - J_c) h_v - p \left[\frac{\partial \alpha_v}{\partial t} + \nabla \cdot (\alpha_v \bar{u}_v) \right]$.

The viscous stress terms are $\bar{V}_l = \nabla \cdot (\alpha_l \bar{\sigma}_l)$ and $V_v = \nabla \cdot (\alpha_v \bar{\sigma}_v)$ which involve the usual Newtonian stress tensor, $\bar{\sigma}_l$ and $\bar{\sigma}_v$, for the liquid and vapor, respectively. We assign the momentum exchange dissipation, Λ , due to drag and phase change to the vapor energy in the form

$$\Lambda = [K + (J_e + J_c)/2](\bar{u}_v - \bar{u}_l)^2,$$

and the viscous work terms are given by $(V_i)_l = \alpha_l \bar{\sigma}_l \cdot (\nabla \bar{u}_l)$ and $(V_i)_v = \alpha_v \bar{\sigma}_v \cdot (\nabla \bar{u}_v)$.

The set of field equations we have discussed above is written in finite difference form for their numerical solution by an extension of the IMF technique. This semi-implicit method allows for all degrees of momentum coupling between the fields, from very loose as occurs in separated flows to very tight coupling as occurs in dispersed flows. It also allows both supersonic and far subsonic or incompressible regions without time step restrictions other than the classical material velocity limitation, $\delta t < \delta x / \bar{u}$. This is accomplished by implicitly treating those terms having to do with signal propagation and interfacial momentum transfer. In addition, experience with two field modeling has shown significant time step advantages by implicitly coupling phase transitions and interfacial heat transfer to the fluid dynamics. Basically, the idea is to implicitly treat all of the interfacial exchange terms and the pressure terms so that at the end of the iteration procedure the velocities, temperatures, densities, and the pressure are all consistent with the effects of the interfacial exchange terms. The importance of this coupling can be pointed out by considering the effects of phase transitions not accounted for in the ICE pressure iteration, and therefore, not influencing the dynamics. Inaccuracies may be introduced in the propagation of compression and rarefaction waves when significant phase change occurs during a single time step. In addition, a large phase change in a single time step may also drive the equation-of-state pressure far from the value arrived at in the pressure iteration; so excessive iterations may be required to solve the implicit equations in the next time cycle. In extreme cases, the pressure can begin oscillating from time cycle to time cycle, and the pressure iteration may eventually fail to converge. Tighter coupling between the pressure iteration and the explicit phase transition can be achieved, which would diminish or eliminate the problems discussed above, by significantly reducing the time step. This would lead to a stable and more accurate solution but the problem computer run time may become prohibitively long.

For many problems in reactor safety analysis, the full two field model may be simplified for a two-phase mixture in the drift approximation. The SOLA-DF (SOLution ALgorithm-Drift Flux) [6] computer code solves the time-dependent, two-dimensional drift flux formulation. If we define the mixture density as the sum of the macroscopic liquid and vapor densities, $\rho_m = \rho_l' + \rho_v'$, the mass average velocity, \bar{u}_m , is defined in such a way that $\rho_m \bar{u}_m$ carries the total momentum of the two-phase mixture, $\rho_m \bar{u}_m = \rho_l' \bar{u}_l + \rho_v' \bar{u}_v$, and a relative velocity, \bar{u}_r , between the two phases as $\bar{u}_r = \bar{u}_v - \bar{u}_l$, then it is straight forward to derive the mixture mass equation

$$\frac{\partial \rho_m}{\partial \tau} + \nabla \cdot (\rho_m \bar{u}_m) = 0, \quad (4)$$

the vapor mass equation

$$\frac{\partial \rho'_v}{\partial \tau} + \nabla \cdot \left(\rho'_v \bar{u}_m + \frac{\rho'_v \rho'_l}{\rho_m} \bar{u}_r \right) = J_e - J_c, \quad (5)$$

the mixture momentum equation

$$\frac{\partial (\rho_m \bar{u}_m)}{\partial \tau} + \nabla \cdot (\rho_m \bar{u}_m \bar{u}_m + \frac{\rho'_v \rho'_l}{\rho_m} \bar{u}_r \bar{u}_r) = -\nabla p + \rho_m \bar{g} + (\bar{V}_v + \bar{V}_l), \quad (6)$$

and the mixture internal energy density equation

$$\begin{aligned} \frac{\partial (\rho_m I)}{\partial \tau} + \nabla \cdot \left[\rho_m I \bar{u}_m + \frac{\rho'_v \rho'_l}{\rho_m} (I_v - I_l) \bar{u}_r \right] = & -\rho \nabla \cdot \left[\bar{u}_m + \frac{\rho'_v \rho'_l}{\rho_m} \left(\frac{1}{\rho_v} - \frac{1}{\rho_l} \right) \bar{u}_r \right] + [K + (J_e + J_c)/2] \bar{u}_r \cdot \bar{u}_r \\ & + \nabla \cdot (k_v \alpha_v \nabla T_v + k_l \alpha_l \nabla T_l) + (V_l)_v + (V_l)_l, \end{aligned} \quad (7)$$

where $I = (\rho'_v I_v + \rho'_l I_l) / \rho_m$.

The equations-of-state and the drift convection of the specific internal energy equation require the knowledge of I_v and I_l . Several possibilities are available:

- (1) Assume that the liquid and vapor phases are at the same temperature, or
- (2) When the heat conduction between phases is small, assume that the vapor phase is at saturation with the local pressure.

Another independent relationship is needed for closure. An expression for the relative velocity \bar{u}_r , can be derived [7] from the momentum equations. Basically, one neglects the phase transition and viscous stress terms, and rewrites the reduced momentum equations in nonconservative form by subtracting from each the proper continuity equation, neglecting phase transition terms. These resulting equations are subtracted from each other yielding transport equations for \bar{u}_r .

We can estimate the drag function K from the drag on an individual bubble (or droplet) times the number of bubbles (droplets) per unit volume, N , by

$$K = \frac{\rho_m S}{8\alpha_1} \left[C_d |\bar{u}_r| \left(\frac{12\nu}{r_0} \right) \right], \quad (8)$$

where

$$\alpha_1 = \alpha, \quad \nu = \nu_l (1 - \alpha)^{-2.5} \quad \text{for } \alpha \leq 0.5,$$

$$\alpha_1 = (1 - \alpha), \quad \nu = \nu_v \alpha^{-2.5} \quad \text{for } \alpha > 0.5.$$

C_d is a drag coefficient (generally of order unity), S is the cross-sectional area per unit volume of bubbles (droplets) with radius r_0 ,

$$S = \begin{cases} \frac{3\alpha}{4r_b} \text{ and } r_o = r_b \text{ if } \alpha \leq 1/2 \\ \frac{3(1-\alpha)}{4r_d} \text{ and } r_o = r_d \text{ if } \alpha > 1/2 \end{cases}$$

and ν is the kinematic viscosity. The average radius is related to the number density by the expressions $r_b = (3\alpha/4\pi N)^{1/3}$ for $\alpha \leq 1/2$ and $r_d = [3(1-\alpha)/4\pi N]^{1/3}$ for $\alpha > 1/2$. The bubble number N is often assumed to be a constant independent of space and time. This, of course, is an approximation that will not work when preferential nucleating sites are desired. Although N must be estimated for each calculation, a locally variable N can sometimes be estimated in terms of a critical Weber number. Modifications to these expressions for more complex flows than individual bubbles or drops are discussed in Ref. [8].

Like K-FIX, SOLA-DF makes use of a semi-implicit formulation in which a variation of the ICE technique is implemented to obtain the numerical solution of Eqs. 4-8.

III. EXAMPLE: CORE-BUBBLE DYNAMICS FOR LIQUID METAL FAST BREEDER ACCIDENT ANALYSIS

Safety analysis of the liquid-metal fast breeder reactor has focused on hypothetical core-disruptive accidents. In one hypothetical scenario, a sudden increase in fuel temperature due to a power burst causes the fuel to melt and vaporize at very high pressures. The expanding bubble of fuel vapor can then vent through the upper core structure into the sodium pool that covers the core region.

The dynamics and energy yield of this bubble ejection must be determined before we can assess the mechanical work that would be done by the sodium pool on the vessel head. The dynamics of the bubble expansion have been simulated by experiments in which a chamber filled with high-pressure air is ruptured and the resulting high-pressure jet of air expands into a water-filled chamber above. Shown in Fig. 1 are frames (courtesy of Argonne National Laboratory) from a high-speed motion picture of one experiment and corresponding plots of marker particle configuration and velocity vector field calculated with K-FIX [5].

As a diaphragm to the high-pressure chamber is ruptured, the surge of air increases the pressure in the water-filled chamber. The momentum imparted to the water leads to an overexpansion of the air and a subsequent drop in bubble pressure. The pressure continues to decrease until 28 milliseconds when the bubble reaches its maximum volume. The bubble begins to collapse into the toroidal shape shown at 40 and 50 milliseconds. During the collapse the bubble pressure increases from the downward-directed momentum of the water. Beyond 50 milliseconds the pressure tends to equilibrate, and the bubble breaks up under the action of turbulence and buoyancy.

The velocity vector field shows a spherical distribution at 10 and 20 milliseconds. At later times, the bubble collapse is evidenced clearly by the reversal of the velocity vectors and the secondary-flow vortex pattern set up between the centerline and outside boundary. The vortex becomes smaller until at 50 milliseconds it is isolated in a corner with most of the velocity vectors directed toward the lower chamber opening.

Calculated and measured pressures in the blowdown vessel, on the base plate and on the vessel head are shown in Fig. 2. Although this example does not make use of the full power of the multifield method, it provides an excellent test of the code's ability to calculate separated two-phase flow in the low Mach number range [9].

IV. EXAMPLE: CRITICAL FLOWS IN TWO-PHASE SYSTEMS

One of the most important phenomena determining the duration of the depressurization, or blowdown, phase of a large-break loss-of-coolant accident is the rate at which coolant exits from the broken pipe. We know from observation that the flow out the break reaches a maximum value independent of the pressure difference between the inside and the outside of the pipe break, provided that the pressure difference is greater than a critical value. This limiting flow phenomenon is called critical, or choked, flow. It is well understood for single-phase compressible fluids, but, at the time we began our study, thermodynamic models and one-dimensional fluid-dynamic calculations of two-phase critical flow often did not accurately predict the observed data. Calculated values of critical flow velocities were usually too large and had to be multiplied by empirically determined factors known as break-flow multipliers to achieve agreement with measured values. Our studies, based on a two-dimensional theory, show that nozzle geometry and nonequilibrium effects must be included to predict the critical flow velocity accurately.

When a single-phase compressible fluid flows through a nozzle, the critical flow velocity equals the speed of sound at the nozzle throat. The physical explanation is simple: When the fluid is moving with the speed of sound, a downstream pressure disturbance propagates upstream as fast as the fluid is moving downstream, so the net propagation of the disturbance is zero. Therefore, under critical flow conditions, the nozzle throat acts as a barrier to any downstream pressure changes. The limiting flow velocity can be altered only by changing the conditions upstream of the throat.

The vapor-liquid mixture, which is also a compressible fluid, exhibits a similar but much more complicated phenomenon. The critical flow velocity is still the sonic velocity at the throat, but the sonic velocity is affected by vaporization along the accelerating flow path, by the spatial distributions of the liquid and the vapor, and by nonequilibrium effects that occur when the liquid phase superheats because of rapid depressurization. The sonic velocity in a homogeneous two-phase mixture can be far less than the sonic velocity in either of the separate single-phase components. This reduction is attributed to the vapor's acting as a weak spring coupled to the large liquid masses.

Equilibrium Two-Dimensional Calculations of Critical Flow Rates

Using a homogeneous equilibrium model [$R = \infty$, $K = \infty$, and $J_e = C(T_l - T_g)$, where C is sufficiently large to maintain $T_l = T_v = T_{\text{saturation}}$], we calculated the critical flow rate for a blowdown experiment at the Semiscale test facility [10]. Semiscale is a small-scale version of a pressurized-water reactor primary system for studying loss-of-coolant accidents resulting from the break of a large cooling pipe. In the experiment that we analyzed, the pipe break was simulated by a nozzle known as the Henry nozzle (Fig. 3). We used the conditions measured a short distance upstream from the nozzle entrance as boundary conditions for our calculations and solved the fluid equations in the immediate neighborhood of the nozzle.

Our initial calculations involved determining the critical flow rate 15 seconds after blowdown began. At 15 seconds, the vapor volume fraction is fairly large and the flow rate is likely to be independent of the vapor production rate, so we assumed an equilibrium phase-change model. In other words, J_e was chosen large enough to maintain the vapor and the liquid at the saturation temperature for each value of the local pressure. The boundary conditions upstream of the Henry nozzle entrance were 48 bars for the pressure, 534 kelvin for the temperature, and 56 kilograms per cubic meter for the mixture density.

We varied the pressure at the nozzle exit between 45 and 10 bars. For selected pressures in this interval, the computations were carried out until the flow reached a steady state, typically at 8 milliseconds after starting the flow from rest. The computed average mass flux and throat pressure are shown in Figs. 4 and 5. Figure 4 indicates that the flow reaches a limiting value as the exit pressure is reduced. The computed critical flow value is in good agreement with the measurements without the use of a break-flow multiplier or any other adjustment. The corresponding one-dimensional calculations also exhibit a critical flow as the exit pressure is reduced, but the computed mass flux must be multiplied by 0.8333 to agree with the data.

To understand the nature of the two-dimensional calculations for a similar experiment in which the Henry nozzle was replaced by the nozzle design used at the LOFT (loss-of-fluid test) facility. Although the abrupt entrance to the throat of the LOFT nozzle (Fig. 6) would seem more likely to exhibit two-dimensional effects than the tapered entrance to the Henry nozzle throat, our one-dimensional results for the LOFT nozzle need only a small correction to agree with the two-dimensional calculation.

We studied the effect of entrance geometry further with a two-dimensional calculation for a Henry nozzle modified so that the entrance to the throat was abrupt rather than tapered. This change in geometry produced only a small change in the mass flow rate and the throat pressure.

Next we investigated the effect of varying the ratio of throat length to throat diameter for the general geometric configuration of the LOFT nozzle. Figure 7 shows the break-flow multipliers required to reach agreement between one- and two-dimensional calculations for various ratios. If the throat length is short relative to its diameter, two-dimensional effects are large. But for ratios greater than about 5, two-dimensional effects are no longer important and the exit flow can be described by a one-dimensional calculation.

A detailed look at the velocity profiles explains this effect. At the throat entrance the radial velocity components are negative and, accordingly, accelerate the central axial velocities. Therefore, a strong radial velocity gradient develops in the entrance region. At a short distance downstream, the radial velocity components become positive and transfer momentum rapidly outward from the center. Here, approximate one-dimensional velocity distributions develop. However, if the throat length is too short for the flow to develop a one-dimensional velocity profile, the one-dimensional models will require a break-flow multiplier to agree with observed data.

Effects of Nonequilibrium Phase Change

The calculations presented so far have corresponded to homogeneous equilibrium phase change. To assess the relative importance of nonequilibrium phase change, we calculated the mass flow rates at the nozzle exit during the first 20 seconds of blowdown using two phase-change models, the equilibrium model described above and a model in which the phase change is zero. Figure 8 shows the calculated values and experimental data for the Henry nozzle. The values were obtained by multiplying the results of a one-dimensional calculation by the calculated break flow multiplier for the Henry nozzle.

During the first 3 seconds of blowdown the fluid entering the nozzle is single-phase liquid. Its temperature is initially 28 kelvin below the saturation temperature, but, as the pressure decreases, the fluid rapidly reaches the saturation point and becomes superheated. The fact that the data lie between the calculated extremes indicates that nonequilibrium phase change occurs during these first few seconds.

After 3 seconds, when a two-phase mixture enters the nozzle, the calculation with equilibrium phase change agrees with the data. Finally, after 10 seconds when the mixture entering the nozzle is mostly steam, the calculated mass flow rates for both vaporization models coincide with each other and agree with the data. The flow rate is independent of the vapor production and is solely determined by the upstream conditions.

To calculate the nonequilibrium effects during the first 3 seconds, we need a detailed model of nonequilibrium vaporization [11]. In a stationary environment, depressurization would lead to vapor production and bubble growth with the growth rate controlled by heat conduction to the bubble surface according to the relation

$$\frac{dr}{dt} = \left(\frac{6}{\pi}\right) \left(\frac{1}{r}\right) \left(\frac{\rho_l}{\rho_v}\right)^2 \alpha_1 \left[\frac{C_1 (T_1 - T_{\text{sat}})}{L} \right]^2 \quad (9)$$

where r is the bubble radius, ρ_l is the microscopic liquid density, ρ_v is the microscopic vapor density, α_1 is the liquid thermal diffusivity, C_1 is the liquid specific heat, T_1 is the bulk liquid temperature, T_{sat} is the

saturation temperature, and L is the heat of vaporization. During the depressurization and acceleration of the fluid through a converging nozzle, the bubble growth rate varies because T_{sat} and ρ_v depend on the pressure and T_1 decreases as heat is used to vaporize the liquid. The instantaneous bubble radius thus depends on the entire bubble history.

The vapor volume fraction α is related to r and N , the number of bubbles per unit of mixture, by

$$\alpha = N \left(\frac{4}{3} \pi r^3 \right) . \quad (10)$$

Combining Eqs. 9 and 10 we derive the following expression for J_e .

$$J_e = \rho_v \frac{\partial \alpha}{\partial t} = \rho_l \left(\frac{18}{\pi} \right) \left(\frac{\alpha}{r^2} \right) \left(\frac{\rho_l}{\rho_v} \right) \alpha_1 \left[\frac{c_1 (T_1 - T_{sat})}{L} \right]^2 . \quad (11)$$

For application to the highly dynamic environment of a critical flow, we retain the form of Eq. 11 but choose a liquid thermal diffusivity and bubble radius that reflect the combined effects of relative motion and turbulence. These modifications allow the model to approach the correct limit in a quiescent environment.

In general, there is a spectrum of bubble radii, but we choose the critical radius for bubble breakup to characterize this spectrum. We determine an initial bubble radius by specifying initial values of N and α . The bubbles grow according to Eq. 9 with α_1 replaced by $\bar{\alpha}$, a liquid thermal diffusivity enhanced by relative motion and turbulence. Consequently, the bubbles grow faster than the conduction-controlled rate. The bubbles continue to grow until they reach a critical size, determined by a Weber number criterion, and then begin to break up. The Weber number characterizes the competition between the dynamic forces that lead to bubble breakup and the restoring force of surface tension. From this point on, the typical bubble radius is taken as the critical radius and the specified initial number of bubbles no longer plays a role.

The critical radius for bubble breakup is given by

$$r_{critical} = \frac{2.3\sigma}{v^2 (\rho_l \rho_v)^{1/3}} , \quad (12)$$

where σ is the surface tension and v is the relative speed between the bubble and the surrounding fluid. To include the contribution of local turbulent fluctuations in the liquid to the relative speed we write v as $v = \beta v_1$, where v_1 is the liquid speed and β is a function of vapor fraction. We choose values of β consistent with observed turbulent velocity fluctuations, which are generally less than 10 per cent of the mean flow velocity. Toward the middle vapor fraction range, β increases because of increased turbulent mixing from the higher shear flow associated with thinning liquid sheets. The increase in β may also result from an increase in the relative velocity.

The enhanced liquid thermal diffusivity $\bar{\alpha}$ that replaces α_1 in Eq. 11 is $\bar{\alpha} = \alpha_1 + Brv$, where B is an empirically determined dimensionless constant. The value of $B = 0.1$ matches the flow rate data for the Semiscale tests. The range of applicability of this value can only be accurately established after extensive data comparisons.

In Fig. 9, the nonequilibrium results for the mass flow rate during blowdown are compared with the data for the Henry nozzle from Fig. 8. The nonequilibrium results agree very well with the measured mass flow rate during the entire period of blowdown. However, at early times the calculated throat pressures (Fig. 10) are higher than the measured wall pressures at the throat entrance. This is believed to result from the combination of nonequilibrium and two-dimensional flow in the proximity of the corner. When subcooled liquid enters the nozzle a nonequilibrium condition may result in the rarefaction region that allows the local pressure to drop slightly below the saturation pressure based on the liquid temperature. When two-phase flow enters the nozzle, however, the increased surface area of contact between the phases and increased mixing result in a much higher flashing rate and hence much less departure from equilibrium. It is important to recognize in comparing pressures that the one-dimensional calculated results yield an area average pressure whereas the data reflect a local wall value close to the corner. Comparisons with mass flow rates, on the other hand, involve integral quantities that should be accurately calculated even in the limited resolution of one-dimension. Figures 11 and 12 show the equilibrium and nonequilibrium calculated results compared with data for the LOFT nozzle of Fig. 6. The agreement with mass flow rates is again very good for the nonequilibrium results. Substantial nonequilibrium exists at early time even with the longer throat length, since the data lie well above the equilibrium results. It is interesting to note that instead of slightly overpredicting the wall pressure in the throat at early time we now slightly underpredict it and the data are much closer to the equilibrium results. The fact that the observed wall pressure at the throat entrance is close to the calculated equilibrium value yet the observed mass flow rate is higher than

the calculated value indicates the occurrence of significant local vapor production near the pressure tap. This detail may well be a consequence of the abrupt entrance combined with a considerably greater distance from the corner to the pressure tap for this nozzle than for the Henry nozzle.

Momentum Exchange

The transfer of momentum between phases in the interpenetrating flow of two materials has been examined by means of an "available-momentum" concept [12]. A transformation of coordinates is made to a system in which the two materials have equal momentum flux into a control volume, and the fraction of lost momentum in that volume is related to the interaction area per unit volume between the materials, f/r , in which f is a dimensionless quantity and r is a measure of the local flow scale. The result of the analysis is a drag coefficient between the liquid and vapor phases,

$$K = \frac{f \rho'_l \rho'_v |\bar{u}_l - \bar{u}_v|}{r(\rho'_l + \rho'_v)}$$

With this type of momentum exchange model, we have observed slip ratios of up to 1.25 for the critical flow simulations. We found that for these calculations, the reported results were relatively insensitive to the form of the momentum exchange function. Since the agreement achieved between the two-dimensional calculations using no slip (mechanical equilibrium) and the Semiscale data was very good, it does not seem warranted to use detailed momentum exchange functions for critical flows. There are, however, other applications where relative velocity effects are important such as downcomer flows [13].

Energy Exchange

We have investigated two approaches for energy exchange. The first is simply thermal equilibrium in which the liquid, vapor, and saturation temperatures are all the same, and the second is the vapor temperature is equal to the saturation temperature corresponding to the local pressure. Once again, the calculated results for critical flows are insensitive to the use of either of these energy exchange models.

Other Critical Flow Studies

In addition to these small-scale tests, the nonequilibrium model has been tested against data obtained from the full-scale critical flow project at the Marviken facility in Sweden (Figs. 13-16), from the low-pressure MOBY DICK loop at the Nuclear Studies Center in Grenoble, France (Fig. 17), and from the low-pressure critical flow loop at Brookhaven National Laboratory (Fig. 18-19). These tests involved fluid pressures from about 90 bars down to slightly greater than 1 bar. Pipe diameters ranged from 75 centimeters down to a few centimeters. We encountered no scaling problems in going from small- to full-scale geometries because the nonequilibrium model is based on local flow and thermodynamic conditions.

Summary of Critical Flow Studies

These studies have proved to be an important contribution in predicting two-phase homogeneous critical flows through nozzles. We have shown that two-dimensional geometric effects not accounted for in one-dimensional calculations reduce the critical flow rates and therefore extend the duration of blowdown. We have also shown the nonequilibrium effects reduce the duration of blowdown because they increase the sound speed and therefore the critical flow rates.

V. EXAMPLE: FLUID-STRUCTURE INTERACTIONS

Pressurized-water reactors operate at relatively high pressure, typically about 150 bars (about 2250 pounds per square inch). Consequently, a sudden break of a large inlet or outlet pipe will produce strong depressurization waves that can create very high transient stresses in the reactor structure. Large-pipe breaks are not expected, even as a result of earthquakes, corrosion, or sudden changes in reactor power. However, reactor systems are designed so that, should one occur, the reactor itself would not be damaged and no significant amount of radioactivity would be released. To determine the margins of safety under these extreme conditions, it is necessary to calculate in detail the dynamic interactions between the fluid and the structural components following a sudden break.

During normal operation, water enters the reactor vessel through an inlet pipe and flows down the downcomer and up through the core (see Fig. 20). The core is separated from the downcomer by a cylindrical steel shell, the core barrel. The core barrel serves a dual function: it holds the fuel codes rigidly in place and separates the cold incoming water from the hot water rising in the core.

Should an inlet pipe break, a depressurization, or rarefaction, wave will propagate into the downcomer at the speed of sound in the water, just under 1 meter per millisecond. As the wave propagates down the downcomer, it leaves a low-pressure region behind it. The resulting high pressure difference across the core barrel causes its outward displacement. In addition, a precursor wave propagates down the core barrel ahead of the main wave in the water (the speed of sound in steel is about 5 times greater than in water), but its effect is small. The motion of the core barrel generates acoustic waves in the water in the core, but their effect also is expected to be small.

These phenomena can be anticipated qualitatively, but in order to quantify them, we need three-dimensional codes for both the complex steam-water flow and the structural motion to calculate the fluid pressure and the stresses in the core barrel.

To model the fluid motion we used a three-dimensional version of K-FIX [14], and to model the core barrel motion, we developed a special-purpose code called FLX [15] that solves the three-dimensional Timoshenko shell equations with an explicit finite-difference technique. (In the earliest work on this problem, the core barrel motion was represented by the classical theory of beams, but we rejected this approximation because, for example, it cannot account for local deformations of the core barrel, particularly where the cylindrical shell bulges toward the break. We also rejected the normal-mode description because it is difficult to formulate mathematically and cannot easily accommodate changes in the boundary conditions or modification to the structure.) Our finite-difference version of the shell equations is relatively straightforward and can be integrated numerically with the very fine time and spatial resolution needed to simulate the complex wave patterns generated by sudden loading.

The coupling of fluid dynamics and structural motion is accomplished in two parts. The fluid-dynamics code computes the pressure gradient acting on the core barrel and this pressure gradient is used in the structural code that solves the Timoshenko shell equations. The motion of the core barrel changes the width of the down-comer and, through this volume change, affects the fluid density. The fluid-dynamics code then incorporates the new density and computes the corresponding flow and pressure fields.

It is not necessary to use the same zoning or time steps in the two codes. In fact, we usually run the structural code with a time step less than a tenth of that used in the fluid-dynamics code because of the relatively high sound speed in the steel core barrel.

In June 1980, the first of a series of experiments was carried out at HDR (Fig. 21). The fuel rods are simulated by a 10-metric-ton ring supported at the bottom of the core barrel. The height of the facility is typical of pressurized-water reactors, but its diameter is considerably smaller.

The response of the HDR core barrel to a guillotine break in a cold leg was monitored with about 75 instruments (pressure gauges, accelerometers, and strain gauges) that had been carefully selected and tested to operate at the temperature and pressure typical of a pressurized-water reactor. The initial temperature (540 kelvin) and pressure (108 bars) were supplied by electric heaters.

Before the experiment was carried out, six United States and West German groups calculated the response of the core barrel to a sudden break and submitted the pretest results to the Kernforschungszentrum Karlsruhe. The Los Alamos predictions [16] for the discharge mass flow rate, pressure distribution, pressure differential, core barrel radial displacement, horizontal and axial strain outside the core barrel are shown in Figs. 22-32. The core barrel undergoes transient oscillation but exhibits no permanent deformation. The figures show good agreement between the Los Alamos calculations and the experimental data.

VI. ACKNOWLEDGEMENT

The work described in this paper was performed under the auspices of the United States Nuclear Regulatory Commission.

VII. REFERENCES

1. M. Ishii, Thermo-Fluid Dynamic Theory of Two-Phase Flow, Eyrolles, Paris (1975).
2. F. H. Harlow and A. A. Amsden, "Numerical Calculation of Multiphase Fluid Flow," *J. Comp. Phys.* 17, 19 (1975).
3. A. A. Amsden and F. H. Harlow, "KACHINA: An Eulerian Computer Program for Multifield Fluid Flows," Los Alamos Scientific Laboratory report LA-5680 (1975).
4. F. H. Harlow and A. A. Amsden, "Numerical Fluid Dynamics Calculation Method for All Flow Speeds," *J. Comp. Phys.* 8, 197 (1971).
5. W. C. Rivard and M. D. Torrey, "K-FIX: A Computer Program for Transient, Two-Dimensional, Two-Fluid Flow," Los Alamos Scientific Laboratory report LA-NUREG-6623 (1977).
6. C. W. Hirt, N. C. Romero, M. D. Torrey, and J. R. Travis, "SOLA-DF: A Solution Algorithm for Nonequilibrium Two-Phase Flow," Los Alamos Scientific Laboratory report LA-7725-MS (1979).
7. J. R. Travis, F. H. Harlow, and A. A. Amsden, "Numerical Calculation of Two-Phase Flows," Los Alamos Scientific Laboratory report LA-5942-MS (1975); also published in *Nuc. Sci. and Eng.* 61, 1-10 (1976).
8. C. W. Hirt and N. C. Romero, "Applications of a Drift-Flux Model to Flashing in Straight Pipes," Los Alamos Scientific Laboratory report LA-6005-MS (1975).
9. J. R. Travis and W. C. Rivard, "Multiphase Fluid Dynamics with Applications in LMFBR Safety Analysis," *Proc. Intern. Mtg. on Fast Reactor Safety and Related Physics*, p. 1511-1519, Chicago, Ill. (1976).
10. J. R. Travis, C. W. Hirt, and W. C. Rivard, "Multidimensional Effects in Critical Two-Phase Flow," *Nuc. Sci. and Eng.* 69, 338-349 (1978).

11. W. C. Rivard and J. R. Travis, "A Nonequilibrium Vapor Production Model for Critical Flow," *Nuc. Sci. and Eng.* 74, 40-48 (1980).
12. B. J. Daly and F. H. Harlow, "Scaling and Constitutive Relationships in Downcomer Modeling," Los Alamos Scientific report LA-7610 (1979).
13. B. J. Daly, "Downcomer Flow Calculations," Los Alamos Scientific Laboratory report LA-7732-SR (1979).
14. W. C. Rivard and M. D. Torrey, "K-FIX: A Computer Program for Transient, Two-Dimensional, Two-Fluid Flow; THREE: An Extension of the K-FIX Code for Three-Dimensional Calculations," Los Alamos Scientific Laboratory report LA-NUREG-6623, Suppl. II (1979).
15. J. K. Dienes, C. W. Hirt, W. C. Rivard, L. R. Stein, and M. D. Torrey, "FLX: A Shell Code for Coupled Fluid-Structure Analysis of Core Barrel Dynamics," Los Alamos Scientific Laboratory report LA-7927 (1979).
16. J. R. Travis, M. D. Torrey, and B. J. Daly, "Blind Calculation of German Standard Problem Number 5," PHDR workshop on GSP No. 5, 2 Dec. 1982, Karlsruhe, West Germany.

FIGURES

Fig. 1. (See last page)

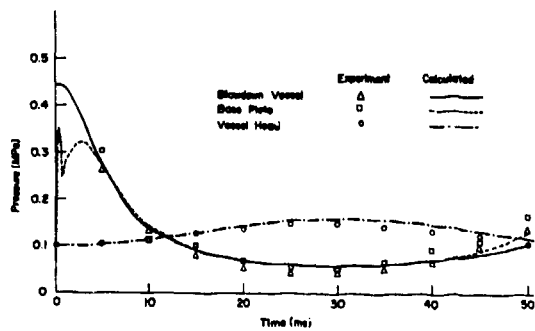


Fig. 2. Comparison of Calculated and Measured Pressures.

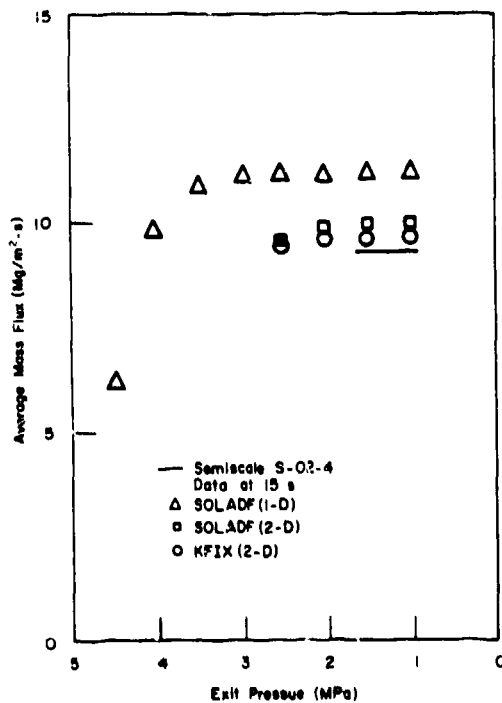


Fig. 4. Computer Average Mass Flux as a Function of the Exit Pressure.

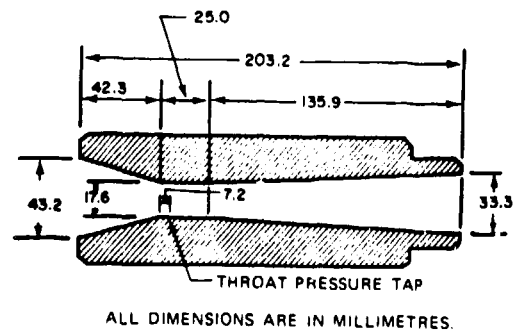


Fig. 3. Henry Nozzle for Semicale Experiment S-02-4. Flow is from Left to Right.

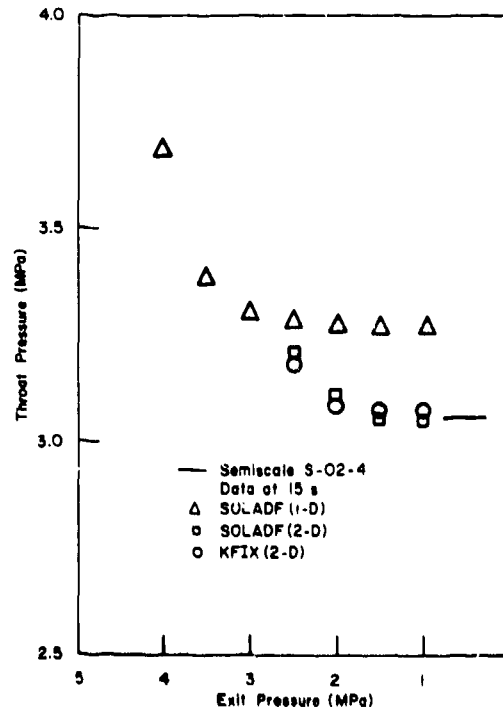


Fig. 5. Computed Throat Pressure as a Function of the Exit Pressure.

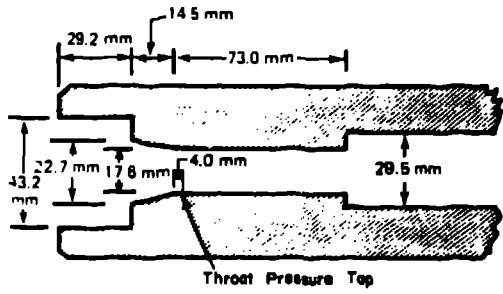


Fig. 6. LOFT Nozzle for Semiscale Experiment S-06-05. Flow is from Left to Right.

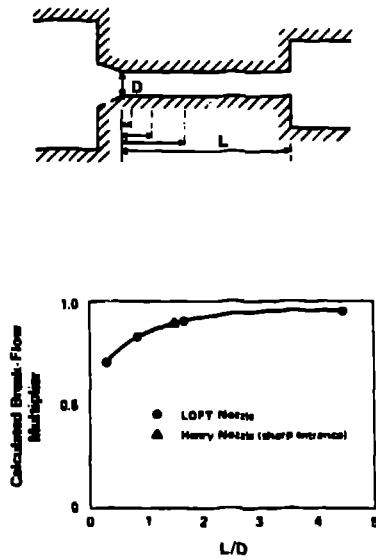


Fig. 7. Effect of the ratio of Throat Length L to Throat Diameter D on the Calculated Break-flow Multiplier.

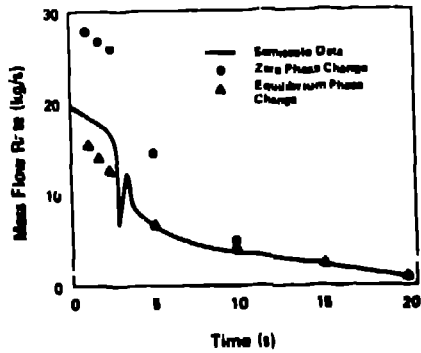


Fig. 9. Measured and Calculated Mass Flow Rates During the First 20 Seconds of Blowdown Test S-02-4 at Semiscale. The Calculations are Based on Two Models, and Equilibrium Phase Change Model and a Model in which the Phase Change is Zero (frozen model).

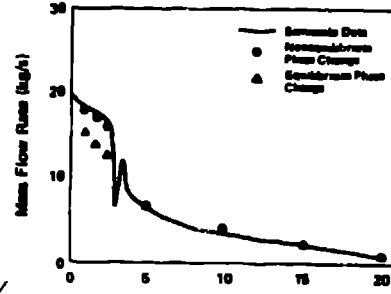


Fig. 9. Measured and Calculated Mass Flow Rates during the first 20 Seconds of Blowdown Test S-02-4 at Semiscale. The Calculations are based on Nonequilibrium (O) and Equilibrium (Δ) Phase Change Models.

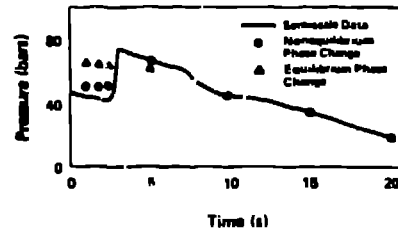


Fig. 10. Measured and Calculated Pressures at Entrance to Nozzle Throat during the first 20 Seconds of Blowdown Test S-02-4 at Semiscale. The Calculations are Based on Nonequilibrium (O) and Equilibrium (Δ) Phase Change Models.

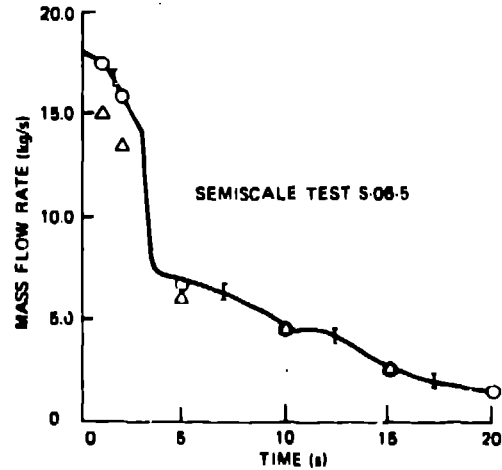


Fig. 11. Measured and Calculated Mass Flow Rates During the First 20 Seconds of Blowdown Test S-06-5 at Semiscale. The Calculations are Based on Nonequilibrium (O) and Equilibrium (Δ) Phase Change Models.

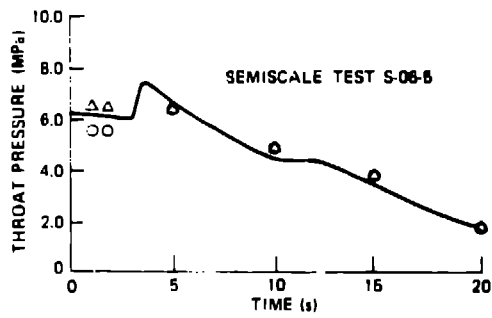


Fig. 12. Measured and Calculated Pressures at Entrance to Nozzle Throat during the First 20 Seconds of Blowdown Test S-06-5 at Semiscale. The Calculations are Based on Nonequilibrium (O) and Equilibrium (Δ) Phase Change Models.

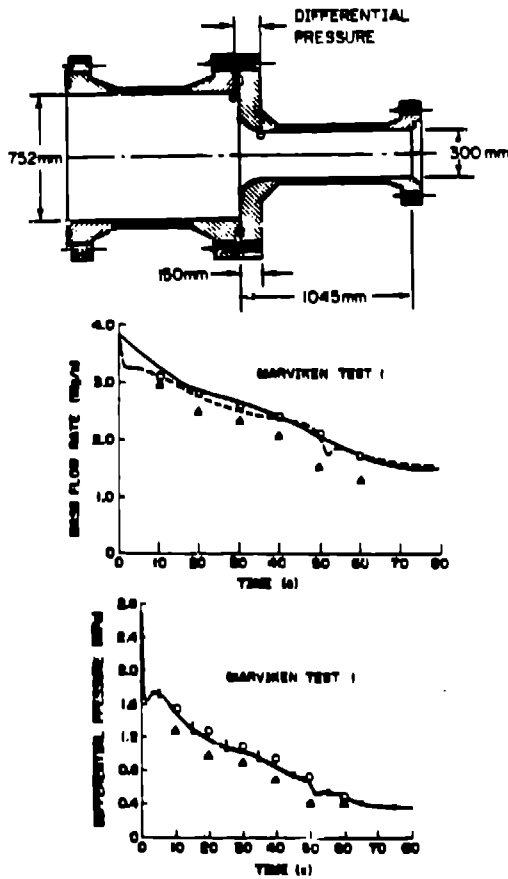


Fig. 13. Marviken nozzle geometry and measured mass flow rates for two different measurement methods and measured differential pressure for Test 1. The Calculated values were obtained for Nonequilibrium (O) and Equilibrium (Δ) vapor production.

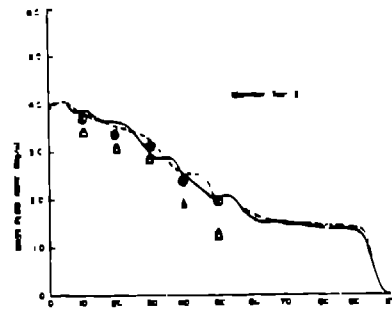
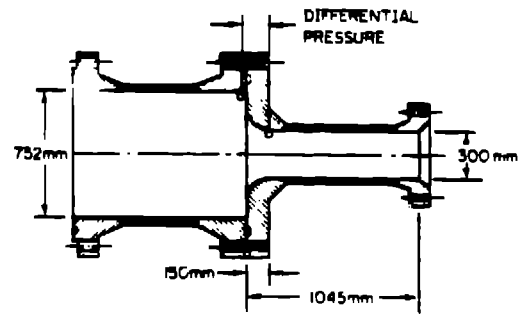


Fig. 14. Marviken nozzle geometry and measured mass flow rates for two different measurement methods for Test 2. The Calculated values were obtained for Nonequilibrium (O) and Equilibrium (Δ) vapor production.

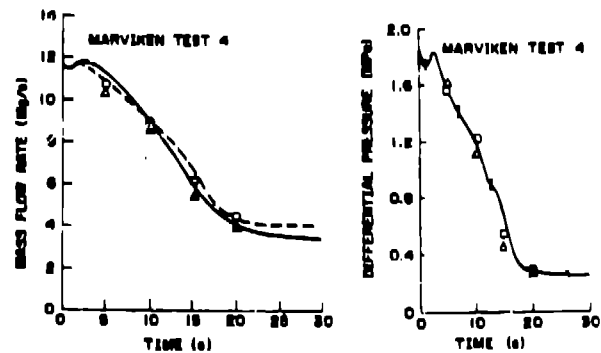
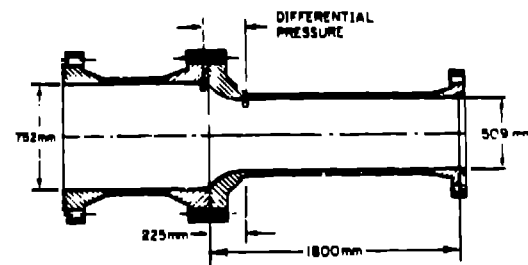


Fig. 15. Marviken nozzle geometry and measured mass flow rates for two different measurement methods and measured differential pressure for Test 4. The Calculated values were obtained for Nonequilibrium (O) and Equilibrium (Δ) vapor production.

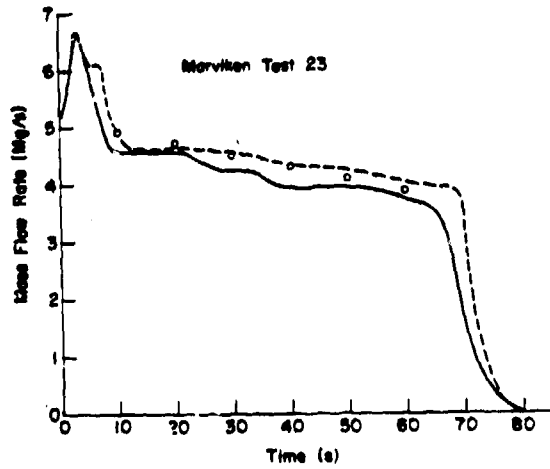
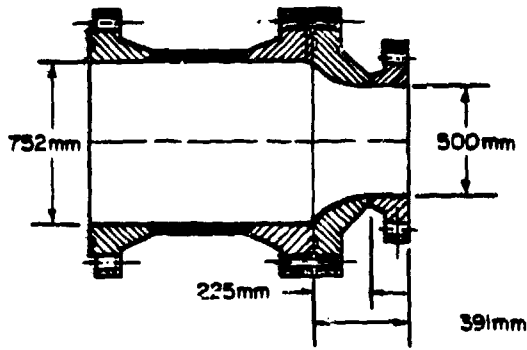


Fig. 16. Marviken nozzle geometry and measured mass flow rates for two different measurement methods for Test 23. The Calculated flow rates were obtained for Nonequilibrium (O) vapor production.

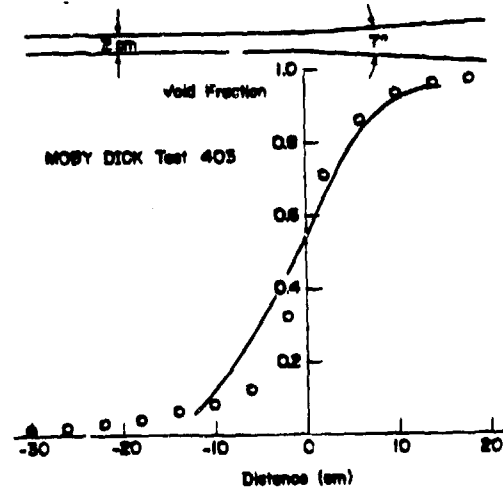
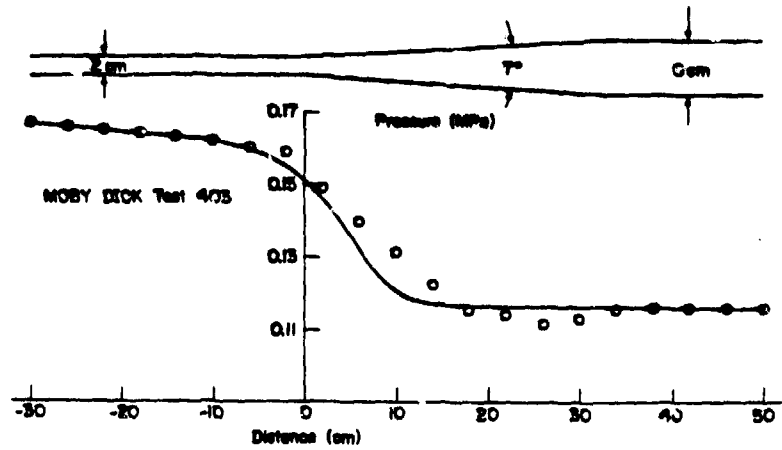


Fig. 17. Moby Dick nozzle geometry and measured axial pressure and void fraction profiles for test 403. The calculated values were obtained for Nonequilibrium (O) vapor production.

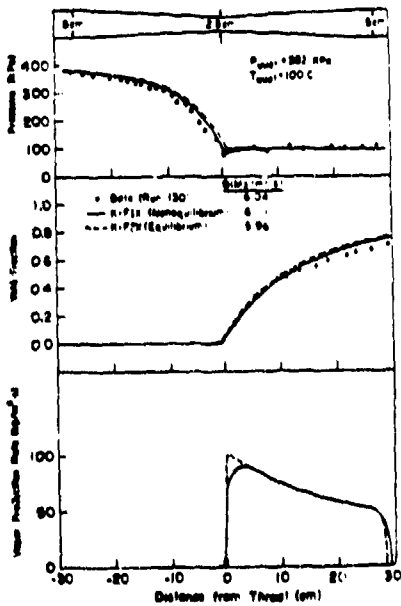


Fig. 18. BNL nozzle geometry and pressure distributions, void fraction profiles, and vapor production rates for test 130.

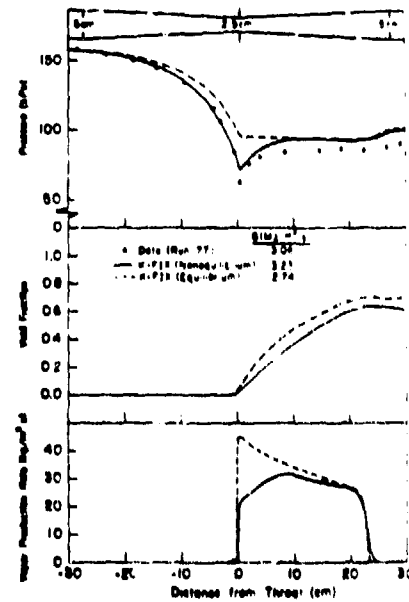


Fig. 19. BNL nozzle geometry and pressure distributions, void fraction profiles, and vapor production rates for test 77.

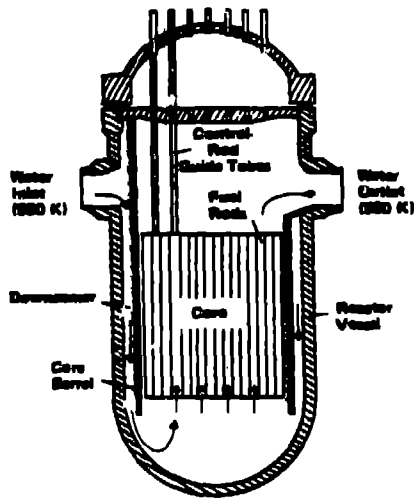


Fig. 20. Schematic Diagram of the PWR Components.

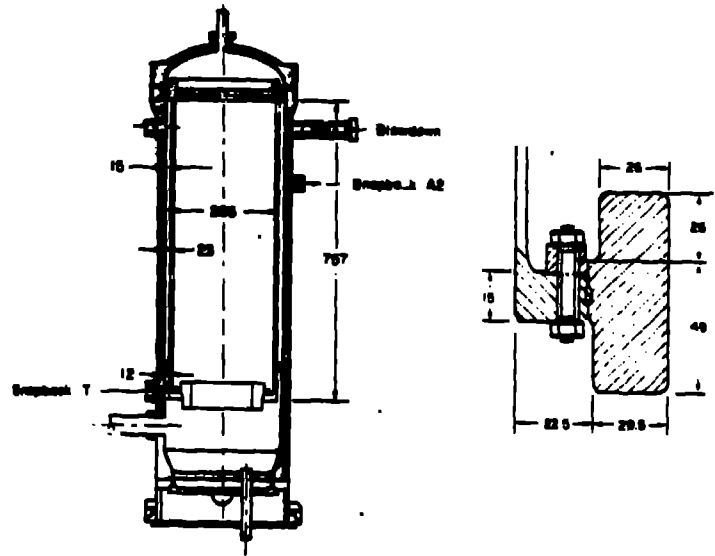


Fig. 21. The HDR Facility (a) at which the Depressurization Experiments were Performed showing the details of Mass Ring (b) which Simulates the Mass of the Fuel Rods. Dimensions are in Centimeters.

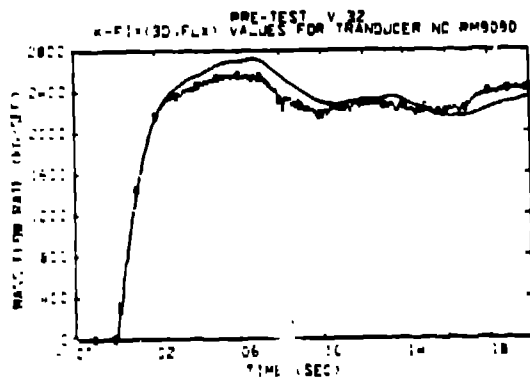


Fig. 22. Pretest calculation (-) of discharge mass flow rate compared with data (D).

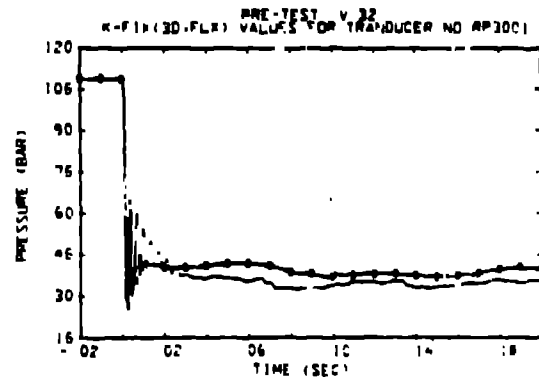


Fig. 23. Pretest calculation (-) of absolute pressure in the blowdown pipe measurement ring compared with data (D).



Fig. 24. Pretest calculation (-) of absolute pressure 25 cm from the end of the blowdown pipe compared with data (D).

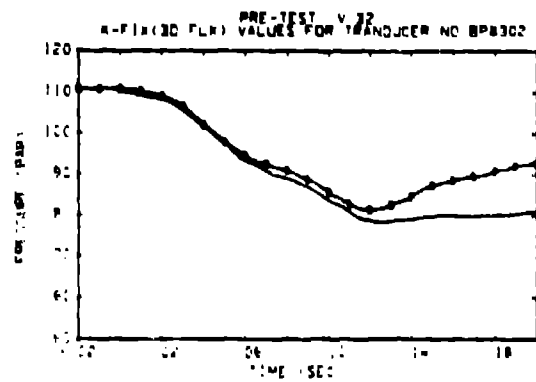


Fig. 25. Pretest calculation (-) of absolute pressure on the vessel axis at the elevation of the blowdown pipe compared with data (D).

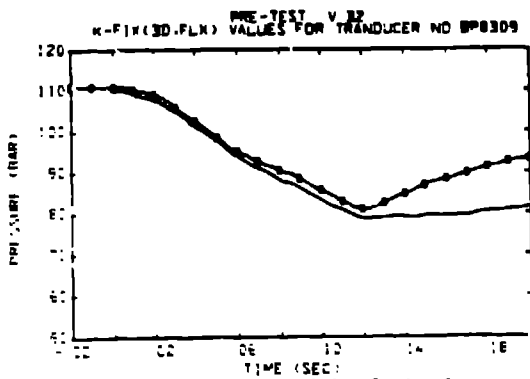


Fig. 26. Pretest calculation (-) of absolute pressure on the vessel axis 299.5 cm below the blowdown pipe compared with data (D).

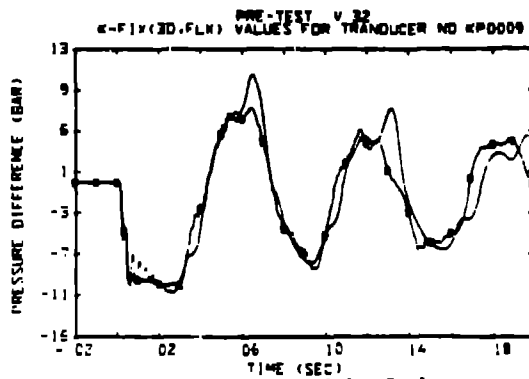


Fig. 27. Pretest calculation (-) of the pressure differential between fluid on the inside and outside of the core barrel at the elevation of the blowdown pipe compared with data (D).

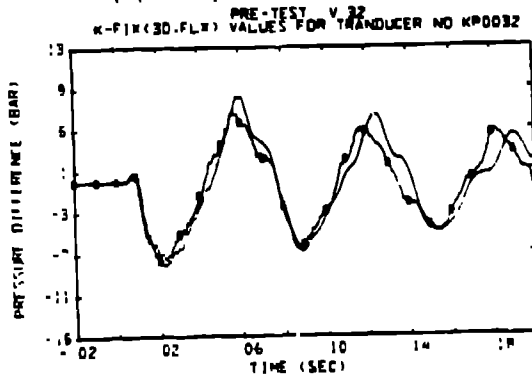


Fig. 28. Pretest calculation (-) of the pressure differential between fluid on the inside and outside of the core barrel at the location 300 cm directly below the blowdown pipe compared with data (D).

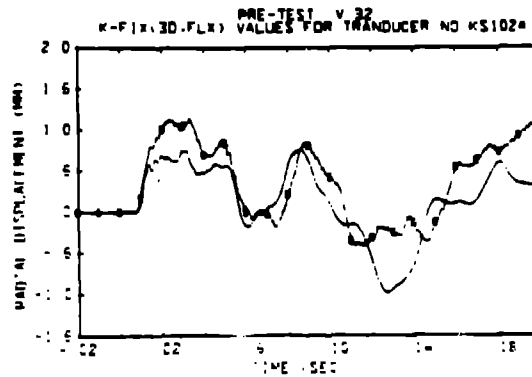


Fig. 29. Pretest calculation (-) of the core barrel radial displacement at the location 330 cm below the 30° around from the blowdown pipe compared with data (D).

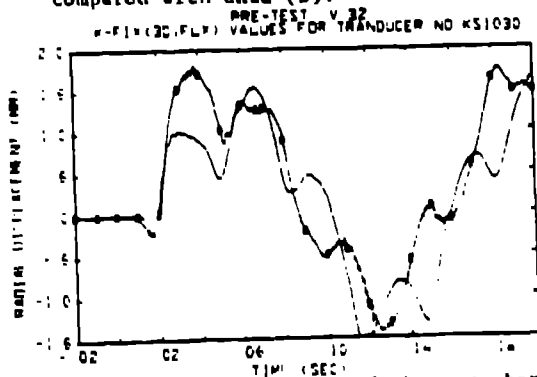


Fig. 30. Pretest calculation (-) of the core barrel radial displacement at the location 655 cm directly below the blowdown pipe compared with data (D).

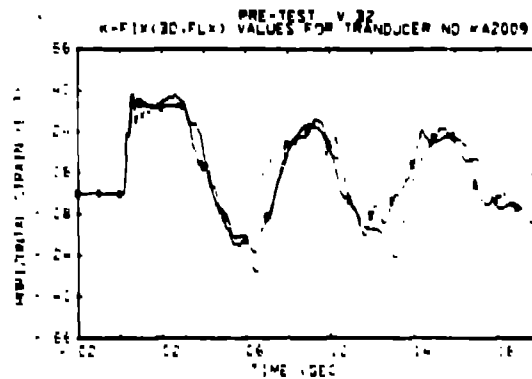


Fig. 31. Pretest calculation of the horizontal strain on the outside of the core barrel at the elevation of the blowdown pipe compared with data (D).

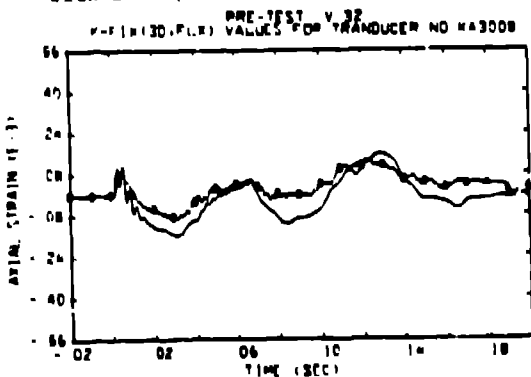


Fig. 32. Pretest calculation of the axial strain on the outside of the core barrel at the elevation of the blowdown pipe compared with data (D).

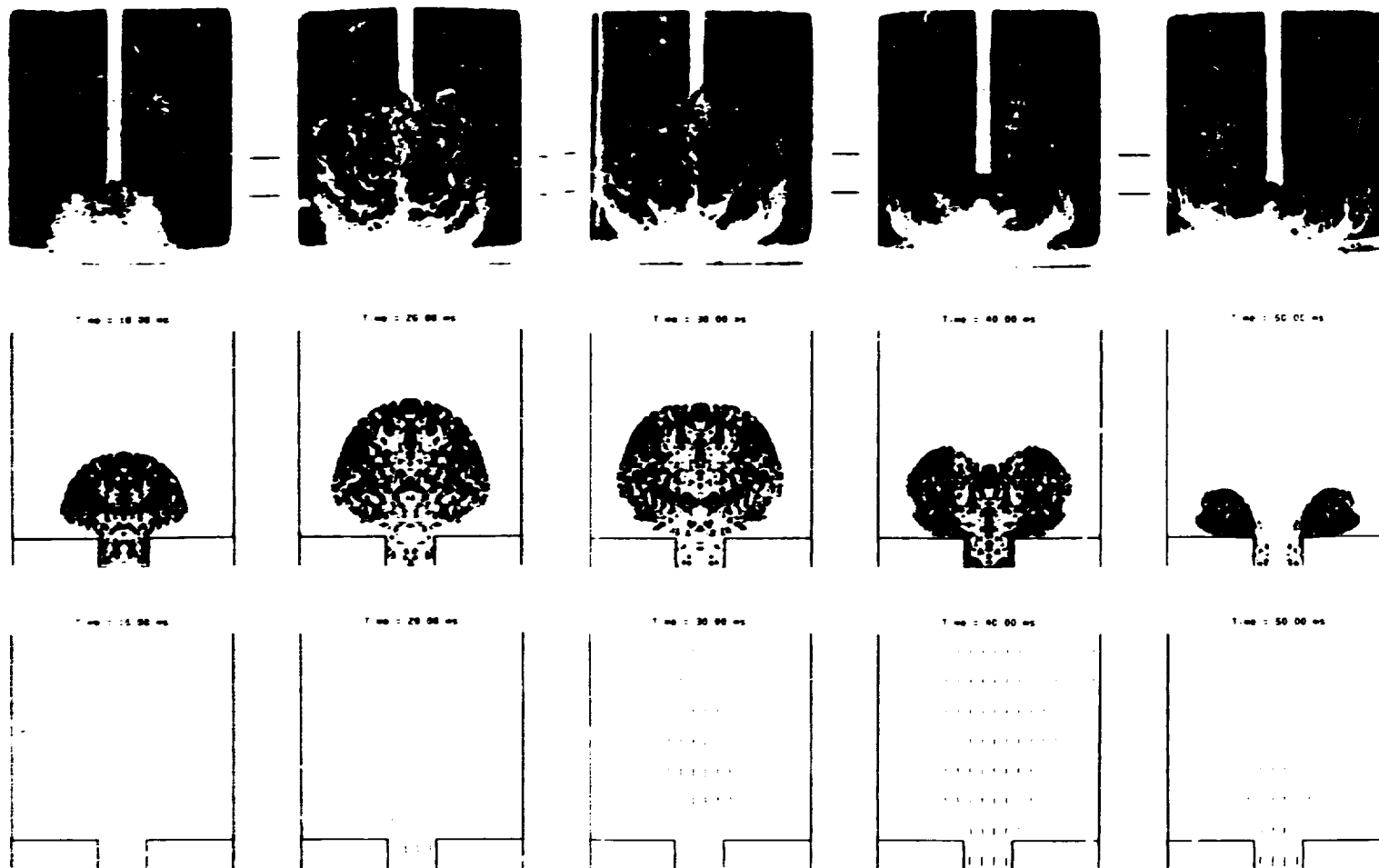


Fig. 1. Frame from the Laboratory Film (courtesy of the Argonne National Laboratory) and calculated marker particle configuration and velocity vectors for 10 ms, 20 ms, 30 ms, 40 ms, and 50 ms.